J. Appl. Comput. Mech., xx(x) (2026) 1-18
DOI: 10.22055/jacm.2026.49060.5712

ISSN: 2383-4536
jacm.scu.ac.ir

Shahid Chamran University of Ahvaz

Journal of Applied and Computational Mechanics

Research Paper

Numerical Simulation and Experimental Investigation of Residual Stress and Distortion in the Repair Welding of a Gas Turbine Nozzle Guide Vane

Mohammad Sajad Rabie Zadeh[1], Esmaeil Hajjari[1], Seyed Mohammad Lari Baghal[1], Ahmad Firouzian-Nejad[2]

[1] Department of Materials Science and Engineering, Faculty of Engineering, Shahid Chamran University of Ahvaz, Ahvaz, Iran

[2] National Iranian South Oil Company (NISOC), Ahvaz, Iran

Received January 05 2026; Revised May 30 2026; Accepted for publication June 23 2026.
✉ Corresponding author: E. Hajjari (e.hajjari@scu.ac.ir)

Abstract. Residual stress and distortion are two important problems that usually arise during the welding of complex industrial components. In this research, the effects of welding heat input, preheating temperature, and mechanical restraints (clamps) on residual stress and distortion in the repair welding of a gas turbine nozzle guide vane are studied through numerical analysis and experimental evaluations. To validate the numerical simulation results, a gas turbine nozzle is practically welded, and the temperature, residual stresses, and distortion are measured experimentally. The simulation results indicate that welding heat input has a significant effect on the distribution of residual stresses. It is observed that preheating does not considerably affect residual stresses, and increasing the preheat temperature leads to an increase in the total distortion of the component. Due to the complex and non-symmetrical geometry of the gas turbine nozzle, using clamps as mechanical restraints does not decrease distortion, but, in most cases, causes an increase in both residual stresses and distortion. The temperature and stress distribution results reveal that the maximum tensile residual stress at the trailing edge adjacent to the weld zone is close to (or exceeds) the yield stress of the base metal. This area experiences a temperature above half of the alloy's melting point, which can satisfy the cracking conditions and lead to the development of liquation and ductility dip cracks.

Keywords: Numerical Simulation, Repair Welding, Gas Turbine Nozzle Guide Vane, Residual Stresses, Distortion.

1. Introduction

The IN738LC nickel-based superalloy is widely used in the hot section of aircraft engines and gas turbines due to its resistance to hot corrosion and high-temperature strength. Exposure to highly corrosive and erosive service conditions at high temperatures leads to various defects due to creep, fatigue, and corrosion, reducing the efficiency of gas turbine components and ultimately requiring repair or replacement [1]. Today, due to increasing raw material costs and the complexity of producing new parts, the demand for repairing damaged gas turbine components has increased. Welding as a repair method has always been highly economical [2]. However, the successful use of welding for repairing complex superalloy gas turbine components remains a major challenge in relevant industries. The main method for repairing parts made of nickel-based superalloys is fusion welding [2-5]. However, using fusion processes for repair welding of complex components such as gas turbine nozzles is usually associated with serious problems such as residual stresses and distortion.

Residual stresses and distortion are the two major concerns in repair welding of gas turbine nozzles. Residual stresses significantly affect the IN-738LC weld and HAZ crack sensitivity [6]. The critical distortion magnitude of the gas turbine nozzle also has to be considered during repair welding, as loss of dimensional accuracy causes problems with assembly in the turbine shell. Distortion arises from non-uniform expansion and contraction of the welded region [7]. Predicting and minimizing residual stress and distortion can result in higher quality and greater productivity. Residual stresses and distortion depend on welding variables such as heat input, preheating temperature, mechanical restraint (clamp type and clamping force), number of welding passes, welding sequence, etc. Finite element modeling and simulation are increasingly used by various researchers for continuous improvement of predictions about the effect of welding process parameters on distortion and residual stresses [8-10].

Malschaert et al. [11] studied the effect of specimen geometry (thickness and length) on residual stresses in T-joints of S355 steel plates welded by two single-pass fillet welds, showing that peak residual stress was two times higher for a 30 mm thick plate than a 10 mm thick plate. In addition, they found that varying the specimen length changed the location of peak residual stress. Dong et al. [12] analyzed residual stresses in repair welding using both experimental measurement and numerical modeling, concluding that the most important parameters influencing repair welding compared to primary welds are heat input, interpass temperature, and number of passes. Song and Dong [13] investigated the effect of repair geometry on residual stress distribution in a dissimilar multi-pass butt-welded joint, finding that residual stresses are distributed asymmetrically in the weld center. Zhao et al. [14] numerically simulated the effect of heat input and number of passes on stress distribution in dissimilar multi-pass welding between S30432 steel and T92 steel, concluding that decreasing heat input and increasing the number of passes reduce maximum residual stress. Heinz et al. [15] studied the effect of preheating and interpass temperature on residual stress in multi-pass welding, concluding that residual stress dependence on interpass temperature is greater than on preheating temperature. Javadi et al. [16] investigated the effect of clamping on residual stress and distortion of Monel plates using numerical simulation, showing that mechanical boundary conditions have a major influence on distortion and lead to nearly a 10% increase in longitudinal residual stress. Sikstrom et al. [17] investigated the relationship between distortion and clamping force in TIG welding of a nickel-based plate, finding that increasing clamping force increases distortion. Jiang et al. [18] evaluated residual stresses and crack propagation in Q690CFD steel welded T-joints using FEM and experimental measurements, demonstrating that heat input significantly impacts the magnitude and distribution of residual stresses and crack propagation. Bonakdar et al. [7] simulated residual stresses in EBW of an IN-713LC gas turbine blade, concluding that increasing beam energy increases the width of the HAZ, the areas exposed to tensile residual stresses, and degree of distortion. Dannis et al. [19] simulated residual stresses leading to cracking during deposition welding of IN738LC superalloy and developed a cracking criterion for determining suitable welding conditions.

Despite recent advancements in welding simulation, the literature still lacks sufficient information regarding the multi-pass repair welding of actual IN-738LC nozzle guide vanes, which are characterized by complex and non-symmetrical geometries. The majority of prior investigations have been conducted on simplified geometries such as plates, T-joints, or beams, and only a limited number of studies have concurrently addressed the combined influence of key welding parameters, including mechanical constraint and preheating, in simulations involving a high number of repair passes. In practical turbine components, critical factors such as geometric complexity, local stiffness variations, and non-uniform mechanical restraints exert a substantial impact on heat transfer, stress evolution, and distortion behavior [7]. Furthermore, inadequate attention has been devoted to establishing correlations between predicted thermo-mechanical fields and the formation of crack-susceptible zones in repaired IN-738LC components. These identified gaps underscore the pressing need for a comprehensive simulation framework that integrates realistic component geometry, multi-pass repair sequences, and relevant process parameters to reliably predict residual stress distributions and distortion in industrial gas turbine nozzles.

This study develops and validates a coupled thermo-mechanical finite element (FE) model, implemented in Simufact Welding software, to simulate the multi-pass repair welding of an industrial IN-738LC gas turbine nozzle guide vane (NGV) with complex geometry. The research systematically investigates the synergistic effects of heat input, preheating temperature, number of welding passes, and arrangement of mechanical constraints (clamps) on the resulting temperature fields, residual stresses, and distortions. The numerical predictions are validated through experimental measurements of thermal cycles, residual stresses, and deformation obtained from industrial-scale repair welding trials. Furthermore, crack-susceptible zones are identified based on the predicted thermo-mechanical fields, enabling the optimization of repair protocols. The primary contribution of this work is the development of a comprehensive simulation framework that accounts for realistic component geometry, multi-pass conditions, and process parameters, thereby providing a basis for minimizing detrimental residual stresses and distortion in the successful repair welding of IN-738LC nozzle guide vanes.

2. Materials, Geometry, and Modeling

The repair welding process was conducted on a used gas turbine nozzle with four blades. As a result of the operation in-service conditions, cracks were created in the middle of the trailing edges of some of the blades. After removing the cracked area (Fig. 1(a)), the nozzle was subjected to repair welding (Fig. 1(c)). For numerical simulations, the cracked gas turbine nozzle was subjected to three-dimensional scanning and its geometrical model was obtained. Afterward, the middle of the trailing edges of the first vane was removed according to the actual dimensions of the crack (Fig. 1(b)).

The weld metal modeling was done using the results obtained from the calibration of the welding heat source to ensure the complete melting of the weld metal. It has been assumed that the repair welding passes produce the same weld metals for all welding heat inputs. The repaired nozzle model has been exhibited in Fig. 1(d).

Fig. 1. (a,b) The removed cracked area at the trailing edge of the first vane of the gas turbine nozzle and its 3D CAD model; and (c,d) the repair welded gas turbine nozzle and the 3D CAD model for the assembled weld metal in the removed area of the gas turbine nozzle.

The HyperMesh software was utilized to mesh the nozzle and weld metal models. 433764 pyramidal tetrahedral elements were used for the nozzle and the distance between nodes was set at a maximum of 2mm, while the minimum size was 0.25 mm (Fig. 2(a)). Brick elements were applied to mesh the weld metal area.

To improve convergence and balance computational accuracy with efficiency, the mesh size in the weld zone was adjusted according to the applied heat input. For heat inputs of 0.132, 0.18, and 0.234 kJ/mm, the distances between nodes were set to 0.4, 0.5, and 0.6 mm, respectively, with sufficient refinement in the fusion zone (FZ) and heat-affected zone (HAZ) (Figs. 2(b) to (d)). This approach exploits the fact that higher heat inputs produce wider fusion and heat-affected zones, which can be adequately resolved with a slightly coarser mesh without compromising the accuracy of macroscopic thermal and mechanical predictions. In this study, the activation of the weld metal elements was performed using the quiet element method based on the thermal criterion of the Simufact welding commercial software [20].

The nozzle and filler metal alloys were IN-738LC and IN-625, respectively, with their chemical compositions given in Table 1. Temperature-dependent thermal and mechanical properties, obtained from JMatPro software and published literature [21, 22], were used to improve simulation accuracy. Both the base and filler metals were modeled using a temperature-dependent elasto-viscoplastic constitutive law with isotropic hardening and the von Mises yield criterion [23]. This formulation was chosen to adequately capture the macroscopic plastic response during multi-pass welding while keeping the computational cost manageable for the complex nozzle geometry. Solid-state phase transformations and detailed microstructural evolution were not explicitly coupled in the mechanical analysis. This simplification is reasonable for IN-738LC because, unlike structural steels, it does not undergo massive solid-state phase transformations that induce significant volumetric strains during the welding thermal cycle. However, this macroscopic approach inherently neglects local microstructural phenomena such as γ' precipitate dissolution, reprecipitation, and the associated local softening or hardening. Consequently, the present model is designed specifically for predicting global thermal histories, macroscopic residual stress fields, and component-level distortion, rather than resolving localized microstructural behaviors.

3. Numerical Simulation

3.1. Thermal and mechanical analysis

The temperature field resulting from the welding process is calculated using the energy conservation equation [24]:

$$k\left(\frac{\partial^2 T}{\partial x^2}\right)+k\left(\frac{\partial^2 T}{\partial y^2}\right)+k\left(\frac{\partial^2 T}{\partial z^2}\right)+S=\rho C\frac{\partial T}{\partial t} \tag{1}$$

where T, k, S, ρ, and C are the temperature, specific thermal conductivity, internal heat generation rate, density, and specific heat capacity, respectively.

The above equation is coupled with the initial and boundary conditions for thermal analysis and solved using the FEM. The incremental relationship between stress and strain is expressed as [24]:

$$d\sigma=[D^{ep}]\,d\varepsilon-[C^{th}]\,dT \tag{2}$$

$$[D^{ep}]=[D^{e}]+[D^{p}] \tag{3}$$

where D^e, D^p, and C^{th} are the elastic, plastic and thermal stiffness matrices, while $d\sigma$, $d\varepsilon$, and dT are the stress, strain and temperature increments, respectively.

3.2. Heat source modeling and calibration

The double ellipsoid volumetric heat source with a Gaussian distribution developed by Goldak [24] was used to simulate the arc welding heat source as shown in Fig. 3.

The heat input has been calculated based on the equation below [24]:

$$Q=\frac{VI\eta}{v} \tag{4}$$

where Q is the input heat (J/mm), I is the current intensity (A), V is the voltage (v), η is the efficiency which is considered 60% for all conditions, and v is the welding speed (mm/s). The Goldak heat source parameters were established through systematic experimental calibration. Bead-on-plate GTAW welds were deposited on the edge of a service-exposed nozzle using IN-625 filler wire at three heat input levels: 0.132, 0.180, and 0.234 kJ/mm. Following welding, the coupons were sectioned via wire-cut electrical discharge machining and prepared metallographically. Cross-sectional macrographs were obtained using an optical microscope. The weld half-width and penetration depth—the key geometric parameters defining the Goldak model—were measured from these macrographs using ImageJ software. The front and rear ellipsoid lengths were subsequently calculated based on the relations reported in Ref. [24]. Table 2 lists the welding conditions and the corresponding calibrated Goldak double-ellipsoid heat source parameters. Simulations were initially performed at all three heat input levels to verify the calibrated parameters against the experimental macrographs. Once validated, these parameters were applied to all subsequent simulations. A direct comparison between an experimental and a simulated weld cross-section is presented in Fig. 4, demonstrating close agreement in the fusion zone geometry.

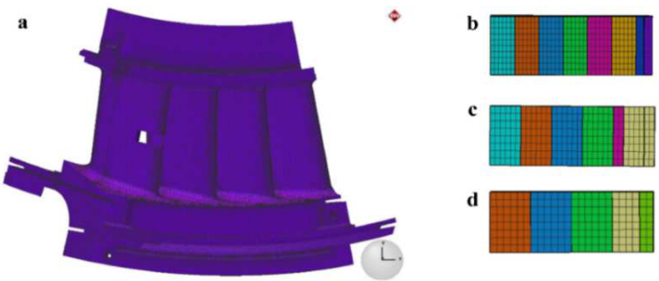

Fig. 2. (a) Mesh geometry of the gas turbine nozzle and (b-d) mesh geometry of the weld metal at different heat inputs: (b) 0.132 [kJ/mm], (c) 0.18 [kJ/mm], (d) 0.234 [kJ/mm].

3.3. Thermal and mechanical boundary conditions

The heat exchange between the welded material and its surroundings during the welding process is considered through both the convection and the radiation and expressed by the following equations, respectively [24]:

$$q_c = h_c\,(T_s - T_\infty) \tag{5}$$

$$q_r = \sigma\varepsilon\,(T_s^4 - T_\infty^4) \tag{6}$$

in the above equations, h_c is the convection heat transfer coefficient, σ is the Stefan-Boltzmann constant, ε is the material radiation coefficient, T_s is the surface temperature, and T_∞ is the ambient temperature. The values used in the thermal boundary conditions are listed in Table 3.

Three mechanical restraint configurations were employed during the welding simulation, as illustrated in Fig. 5. In the no-clamp configuration (Fig. 5(a)), rigid body motion was suppressed by fully constraining four nodes on the right side of the nozzle platform. In the Type I clamp configuration (Fig. 5(b)), a rigid clamp (17 × 100 × 5 mm) was placed on the upper part of the nozzle; the contact was modeled as rigid-to-flexible and frictionless, with the clamp acting solely as a geometric constraint without any applied clamping force. In the Type II clamp configuration (Fig. 5(c)), a rigid clamp of identical dimensions was applied to both sides of the platform under a force of 2000 N per side, utilizing frictionless pressure-type contact. In all configurations, friction was omitted because thermal contraction mismatch—rather than interfacial shear—is the dominant mechanism driving residual stress and distortion in this application. Including friction would increase computational cost without providing meaningful improvement in accuracy.

3.4. Numerical solution

The numerical solutions of temperature and stress fields were conducted in nine cases with different welding conditions using the coupled thermo-mechanical FEM by the Simufact welding software. The calculation process consists of two stages: thermal and mechanical analyses. The simulation variables including heat input, mechanical constraints, and preheating temperature are listed in Table 4. In all conducted analyses, the average welding speed was set to 0.5 mm/s and the welding efficiency was considered as 0.6. It was also assumed that the base metal is free from initial stress in all simulation modes.

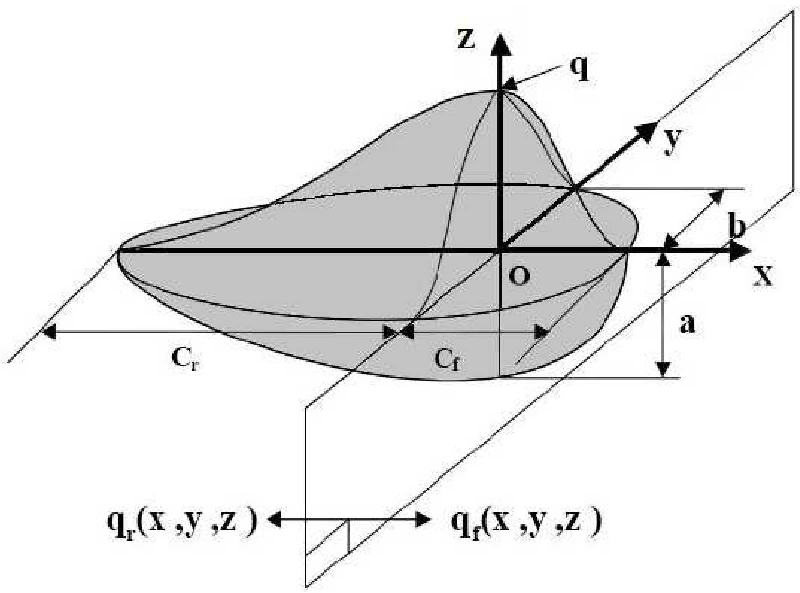

Fig. 3. Schematic of goldak double ellipsoid heat source parameters.

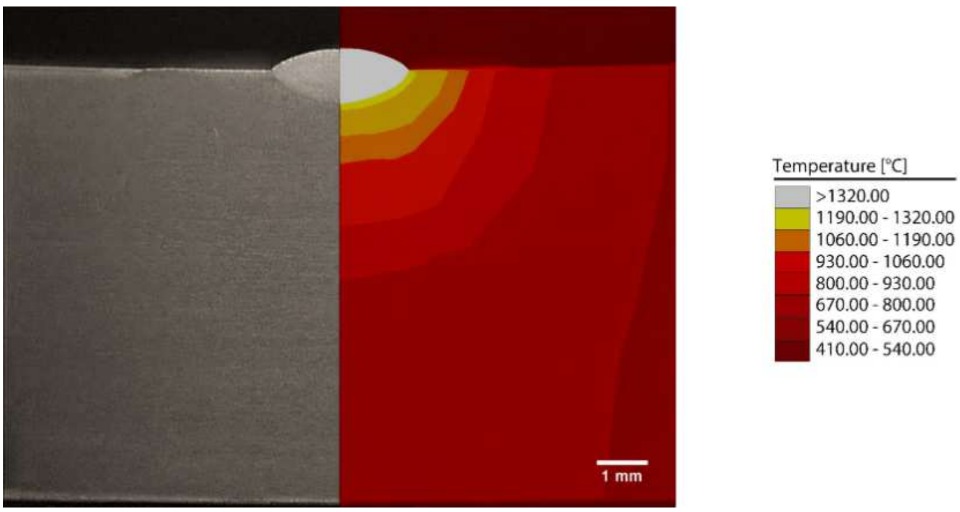

Fig. 4. Comparison between the experimental macrograph and the simulated fusion zone cross-section.

Table 1. Chemical composition of the IN-738LC nozzle and IN-625 filler metal (wt.%).

Material	Ni	S	Si	Mn	Fe	Zr	Ti	Cu	Al	Nb	Ta	W	Mo	Cr	Co	C
IN-738LC	Bal.	-	0.09	0.013	0.0131	0.047	3.1	0.5	3.26	0.9	1.61	2.6	1.76	16.09	9.08	0.09
IN-625	Bal.	0.015	0.5	0.5	5.0	-	0.4	0.5	0.4	3.00	1.15	2.54	8.0	21	2	0.1

Table 2. Welding conditions and Goldak double-ellipsoid heat source parameters for each test.

Test No.	Current (A)	Voltage (V)	Heat input (kJ/mm)	Half-width (mm)	Depth (mm)	Rear length (mm)	Front length (mm)
1	20	5.5	0.132	3.85	1.56	7.70	3.85
2	25	6.0	0.180	4.42	1.82	8.84	4.42
3	30	6.5	0.234	5.20	2.10	10.40	5.20

Table 3. Thermophysical properties of IN-738LC and IN-625 alloys used for thermal boundary conditions [21, 22].

Material	Stefan-Boltzmann constant ($W.\ m^{-2}.\ K^{-4}$)	Ambient temperature (°C)	Radiation coefficient	Convection heat transfer coefficient ($W.\ m^{-1}.\ K^{-1}$)
IN-738LC	5.67×10^{-8}	25	0.6	15
IN-625	5.67×10^{-8}	25	0.8	25

Table 4. Simulation cases of the gas turbine nozzle repair welding.

Case No.	Type of constraint	The initial temperature of the part (°C)	Heat input (kJ/mm)
1	Without clamp	25	0.132
2	Without clamp	25	0.180
3	Without clamp	25	0.234
4	Without clamp	200	0.234
5	Without clamp	400	0.234
6	Without clamp	600	0.234
7	Clamp Type I	25	0.234
8	Clamp Type II	25	0.234
9	Clamp Type II	400	0.234

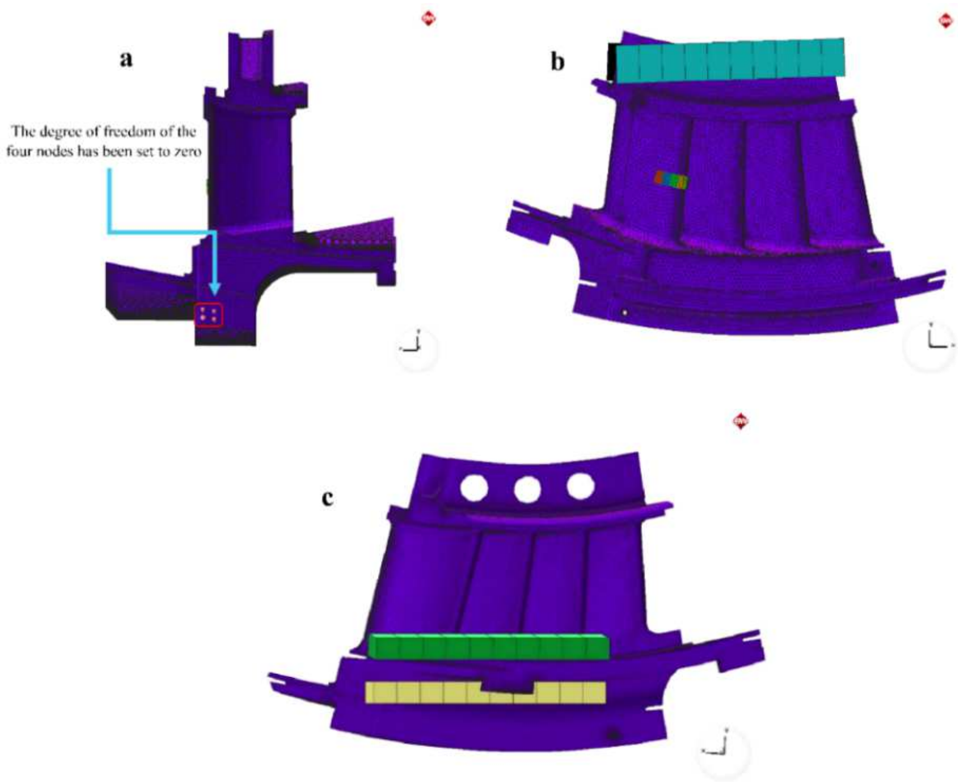

Fig. 5. Mechanical boundary conditions used in the simulation of the repair welding of the gas turbine nozzle (a) the degrees of freedom of the four specified nodes are equal to zero, (b) the upper part of the nozzle is restrained by clamps (Type I), (c) the platform of the nozzle is restrained by clamps (type II).

The number and spatial distribution of repair welding passes for each heat input level are illustrated in Fig. 6. In this figure, the black arrows indicate the welding torch angle during the simulation, while the brown regions represent the volume of the Goldak heat source. The total numbers of repair welding passes for heat inputs of 0.132, 0.18, and 0.234 kJ/mm were 52, 34, and 27, respectively. For each heat input level, the number of passes and the inter-pass time/temperature were determined from the calibrated heat source parameters to ensure complete melting of the weld metal and stable convergence of the numerical solution.

The total numbers of repair welding passes for heat inputs of 0.132, 0.18, and 0.234 kJ/mm were 52, 34, and 27, respectively. The number of welding passes and the inter-pass time/temperature for each heat input were selected based on the results of the calibration of the molten pool parameters and the trial-and-error method to ensure the complete melting of the weld metal and the convergence of the numerical solution.

In this research, the numerical solutions were performed using a powerful 12-core server with an Intel Core i7 8700K CPU and 64 GB of RAM. The shortest process time was 11 hours for the heat input of 0.234 kJ/mm and the longest was 25 hours for the heat input of 0.132 kJ/mm.

4. Experimental Procedure and Verification

To validate the results obtained from the numerical simulation for temperature distribution, residual stresses distribution, and distortion, a gas turbine nozzle was practically subjected to the repair welding process. The nozzle was welded using the GTAW process with constant current and negative polarity. The welding parameters were selected according to the ninth case of Table 3. Measurements were constrained to a single weld sample by the experimental setup and available resources. The validated case (e.g., Case 9) was chosen because it represents an intermediate and critical condition within the welding parameter range. Validating this case provides reasonable confidence in the model's predictive capability for the other cases. Before welding, solution annealing was performed for 2 hours at 1200 °C to dissolve the gamma prime precipitation phases, and then the desired cracked area was removed for repair welding (Fig. 1(a)). The nozzle was preheated using an electric furnace. After taking out the sample from the furnace, the sample was placed on a clamp, and to prevent contact heat transfer, a refractory blanket was applied at the contact area between the clamp and the sample. The filler metal IN-625 with a diameter of 0.8 mm was used to fill the removed area. During the welding process, the nozzle temperature was recorded using an infrared thermometer (Fig. 7). Owing to the complex geometry, the placement of thermocouples and the measurement of temperature at multiple locations of the nozzle were not feasible. Therefore, experimental nozzle temperature measurement was conducted at a single point on the nozzle.

After the repair welding process, the gas turbine nozzle was subjected to visual inspection and fluorescent penetrant inspection (FPI) to reveal probable cracks and/or other imperfections created due to the welding process. The repair welded nozzle is shown in Fig. 1(c).

The hole drilling technique was applied for experimental measurement of residual stresses in the welded nozzle and validating of the calculated residual stresses obtained from the FEM (Fig. 8). This process was conducted based on the ASTM E837 standard [25]. Due to the small thickness of the nozzle vane, the stress was not measured in depth and the surface stresses were measured in two directions parallel to and perpendicular to the weld line. Due to the confined nature of the welded region of the nozzle, access for the drilling setup was restricted, and the installation of strain gauge rosettes at multiple points was not feasible. Consequently, experimental residual stress measurement using the hole-drilling method was carried out at only one point on the nozzle.

The distortion generated by repair welding process of the gas turbine nozzle was experimentally measured using a coordinate measuring machine (CMM) before and after welding process.

Figure 9 shows the locations for experimental measurement of temperature and residual stresses on the gas turbine nozzle for comparison with the numerical simulations. Descriptions of the locations specified in Fig. 9 are given in Table 5.

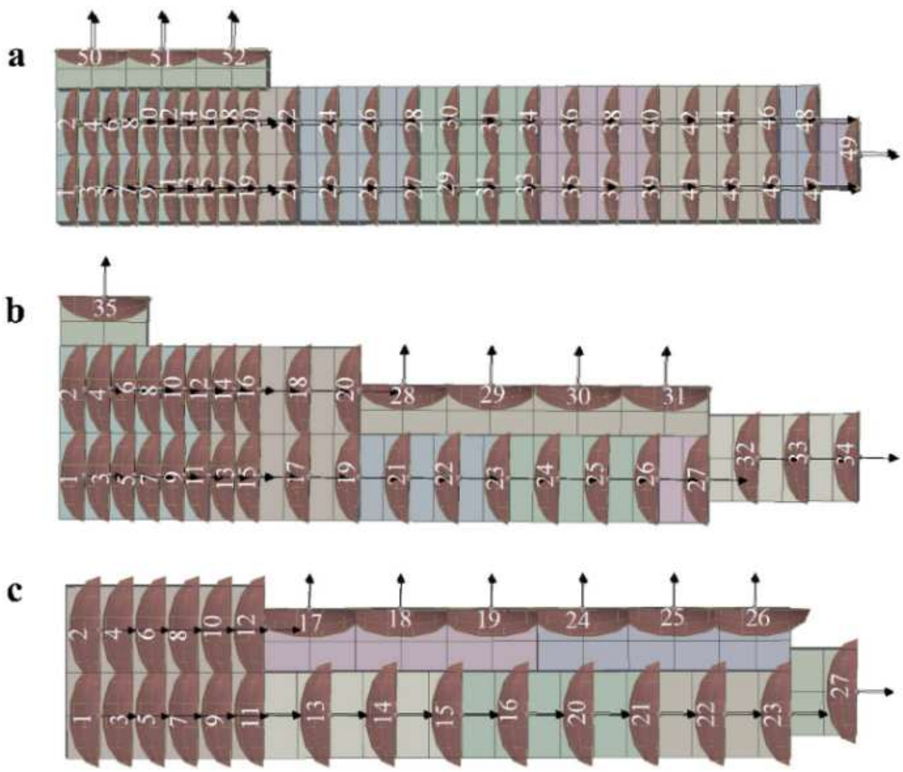

Fig. 6. Schematic top view of the weld metal and the welding passes for different heat input levels, (a) 0.132 kJ/mm, (b) 0.18 kJ/mm, (c) 0.234 kJ/mm.

Table 5. Guide to Fig. 9.

Point A	The location of the experimental temperature measurement in repair welding of the gas turbine nozzle
Point B	The location of the experimental residual stresses' measurement in repair welding of the gas turbine nozzle
Path 1	The path for the extraction of the structural simulation results
Path 2	The path for the extraction of the structural simulation results

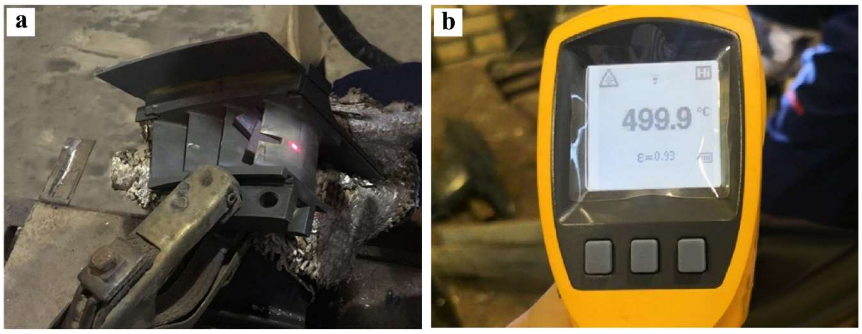

Fig. 7. Experimental measurement of temperature during repair welding process of the gas turbine nozzle (a) gas turbine nozzle before welding process, (b) recording temperature during welding process.

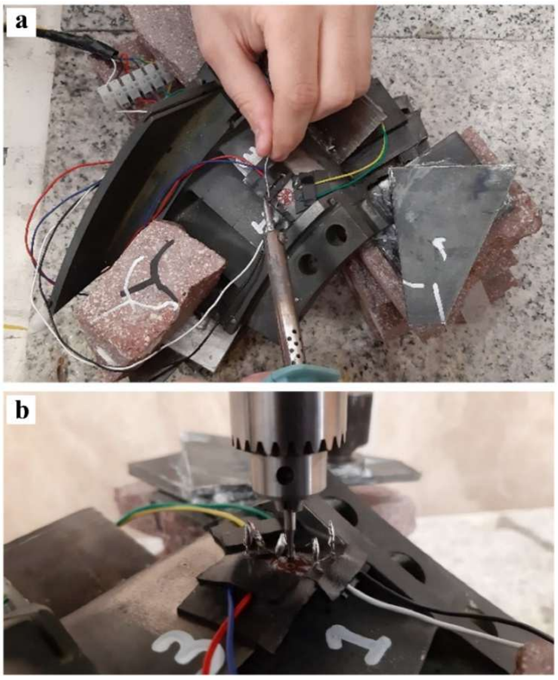

Fig. 8. Experimental measurement of residual stresses in the welded nozzle via hole drilling technique (a) establishing the connections between strain gauges and data logger to measure residual stresses, (b) drilling the nozzle sample.

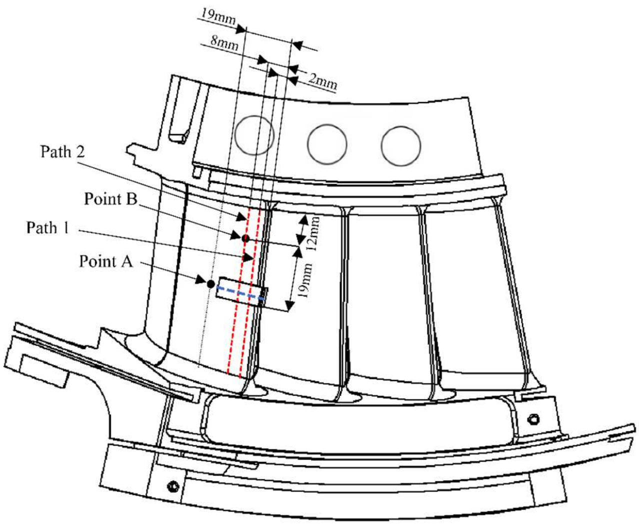

Fig. 9. Location of the temperature and residual stresses measurement in numerical simulation and experimental repair welding of the gas turbine nozzle.

5. Results and Discussion

5.1. Results of thermal analysis

Figure 10 illustrates the numerically obtained temperature history in multi-pass repair welding of the gas turbine nozzle at a distance of 5 mm from the weld metal (point A in Fig. 9). Figs. 10(a) to (c) and 10(d) to (f) correspond to cases with different heat inputs and different preheating temperatures, respectively. The time-temperature diagrams in each welding pass, consist of three parts. The first part shows the temperature rise due to a new welding thermal cycle. The second shows the maximum temperature at the selected point, and the third part the temperature drop due to separation of the heat source and the cooling of the nozzle under the defined environmental conditions.

As shown in Figs. 10(a) to (c), when the heat input increases, the maximum temperature at the corresponding node also increases. On the other hand, based on the diagrams shown in Figs. 10(d) to (f), applying preheat and raising its temperature, increases the peak temperature during the first 16 passes. Eventually, the nozzle temperature decreases after the 17th pass. Also, the heating and cooling rates of the nozzle in the cases where the preheating is utilized are lower than those without preheating.

In Fig. 10(e) the comparison between experimentally and numerically determined thermal cycles at the specified location at a distance of 5 mm from the weld zone is presented.

Despite some occasional differences, the measured maximum and minimum temperature changes in the experimental repair welding are in good agreement with the results obtained from the FE simulation using Simufact welding software. The maximum error between the simulation results and the experimental measurements is about 15%. Unlike the simulation, the actual manual welding process results in non-uniform pass shapes. In addition to the above factors, the differences in thermal and mechanical boundary conditions between the numerical simulation and the experiment can contribute to this deviation in the thermal cycles.

Figure 11 illustrates the numerically predicted temperature fields at 297 s of the welding process for different preheating conditions. Figs. 11(a), (b), (c), and (d) correspond to cases 3, 4, 5, and 6, respectively. As the preheating temperature increases, the area around the initial welding passes experiences higher temperatures. Furthermore, the preheating process reduces the temperature gradient near the welding zone. However, due to the specific geometry of the nozzle, increasing the preheat temperature leads to a non-uniform temperature distribution throughout the workpiece, particularly at the bottom and near the platform.

5.2. Results of mechanical analysis

5.2.1. The effect of the heat input on the residual stresses

Figure 12 shows the numerically predicted distribution of the longitudinal residual stresses (stress results in the Y direction) after the final cooling of the nozzle welded at different heat inputs. Figs. 12(a), (b), and (c) are related to cases 1, 2, and 3, respectively. As can be seen, the longitudinal residual tensile stresses in the HAZ and the base metal increases by moving from the starting point of the welding to the trailing edge of the vane, and the maximum longitudinal residual tensile stress in the HAZ region is created exactly at the trailing edge of the vane. On the other hand, the longitudinal residual stresses at the end of the removed area (the starting point of the welding) are mainly compressive. Based on the results shown in Fig. 12, increasing the welding heat input increases the area with longitudinal residual compressive stress.

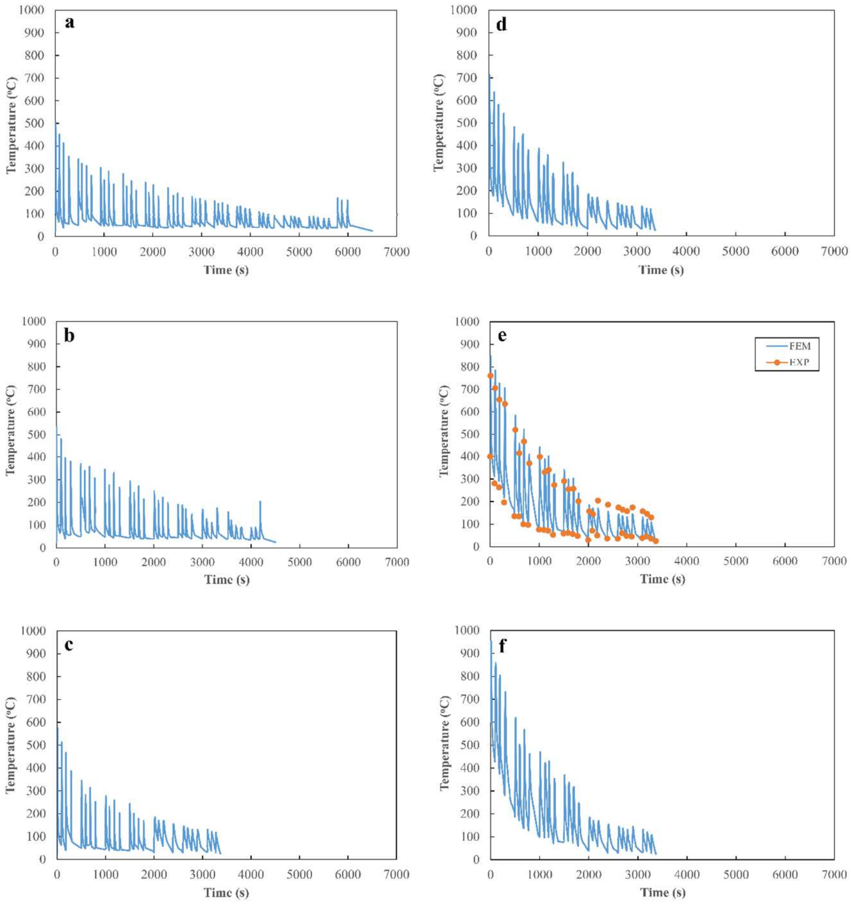

Fig. 10. Temperature history in the multipass repair welding of the gas turbine nozzle at a distance of 5 mm from the weld metal (point A in Fig. 8). (a) Case 1, (b) case 2, (c) case 3, (d) case 4, (e) case 5, and (f) case 6.

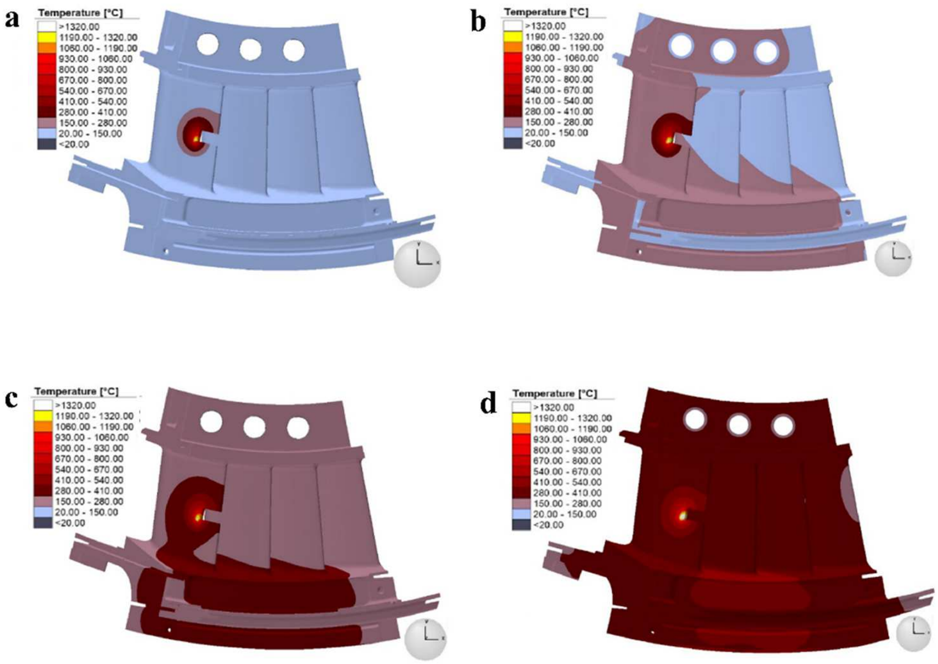

Fig. 11. Numerically predicted temperature fields at 297 s of the welding process for different preheating conditions (a) case 3, (b) case 4, (c) case 5, (d) case 6.

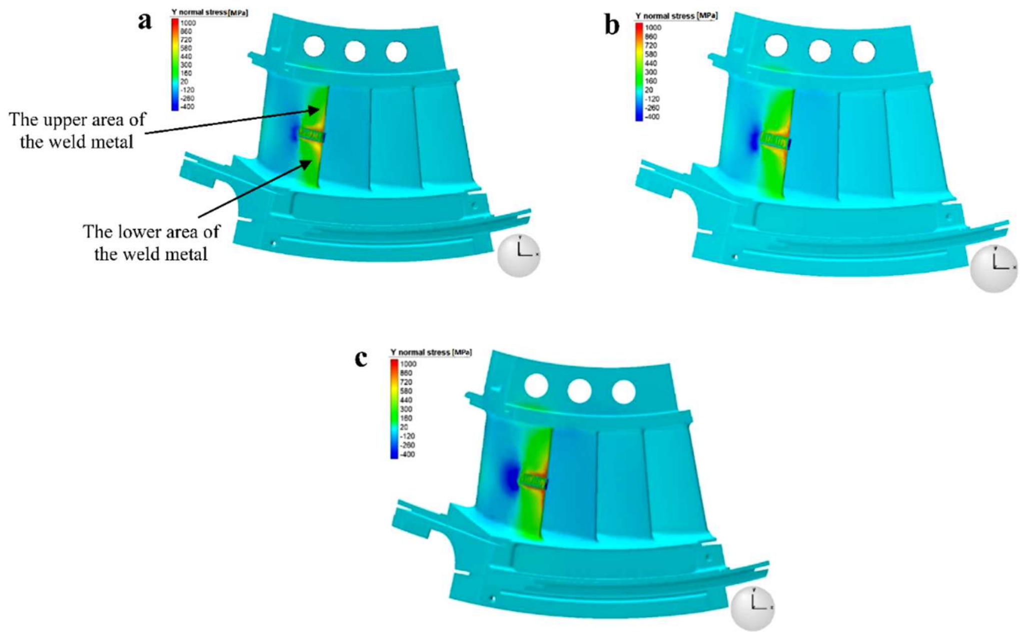

Fig. 12. Distribution of longitudinal residual stresses for the repair welding of the gas turbine nozzle at different heat inputs (a) 0.132 kJ/mm, (b) 0.18 kJ/mm, (c) 0.234 kJ/mm.

To further investigate the effect of the heat input, preheat temperature, and the mechanical boundary conditions, the numerically obtained longitudinal residual stresses caused by the repair welding process were extracted along a straight path near the end of the repaired area (path 1). The exact location of this path is illustrated in Fig. 9.

Fig. 13 shows the changes in the longitudinal residual stress for different welding heat inputs along path 1. As can be seen, in most points of the diagrams, the highest tensile longitudinal residual stresses are related to the heat input of 0.234 kJ/mm, and the lowest tensile longitudinal residual stresses are associated with the heat input of 0.132 kJ/mm. According to the diagrams in Fig. 13, for path 1 the tensile longitudinal residual stresses in the HAZ are considerably higher than those in the weld metal. Based on the obtained results, the values of the maximum tensile longitudinal residual stresses in the HAZ of the welded samples with 0.132 kJ/mm, 0.18 kJ/mm, and 0.234 kJ/mm heat inputs are 669, 680, and 710 MPa, respectively. Such high levels of tensile longitudinal residual stresses near the thin trailing edge of the vane can make this zone highly susceptible to solidification cracking, ductility dip cracking, and liquation cracking.

According to the results obtained in this research, heat input significantly affects the distribution of residual stresses during the repair welding of the gas turbine nozzles. The main feature of the welding heat input is its direct effect on the cooling rate. As the heat input increases, the tensile longitudinal residual stresses created by the welding process are increased due to an increase in the applied energy and thus the creation of higher temperature gradients. The high dependency of the residual stress distribution on the welding heat input has also been reported by other researchers [15, 19, 26].

For the heat input of 0.18 kJ/mm and 0.234 kJ/mm, the tensile longitudinal residual stresses in the center of the weld metal are at a maximum and decrease when moving away from the upper and lower edges of the weld metal the residual stresses are decreased. The high tensile longitudinal residual stresses in the center of the weld metal can lead to solidification cracking, ductility dip cracking, and liquation cracking in this zone of the welded samples.

5.2.2. The effect of preheating on the residual stresses

Figure 14 shows the longitudinal residual stresses distribution along path 1 for the constant heat input (0.234 kJ/mm) and different preheating temperatures. According to the diagrams shown in Fig. 14, the greatest impact of the preheating treatment is observed on the longitudinal stresses in the center of the weld metal. The maximum value of tensile longitudinal residual stress in the center of the weld metal in the non-preheated condition is 200 MPa, while the application of preheating treatment at 600℃ has caused an increase of about 162% in the tensile longitudinal residual stresses compared to the non-preheated condition. In contrast to the weld metal, the impact of the preheating treatment on the tensile longitudinal residual stresses in the HAZ is almost negligible. According to the results presented in Fig. 14 for the non-preheated condition, the maximum tensile longitudinal residual stresses in the HAZ at the upper half of the welded vane are about 710 MPa (80% of the yield stress of the base metal), which changes to 735, 715 and 660 MPa due to the preheating treatment at 200℃, 400℃ and 600℃, respectively. As can be seen, preheating at 200℃ increases the tensile longitudinal residual stresses in this area by about 3.5% compared to the non-preheated condition. However, increasing the preheating temperature to 600℃ reduces the tensile longitudinal residual stresses in this area by about 7% relative to the non-preheated state. Preheating and increasing the preheating temperature have a non-linear effect on the trend of the residual stress changes in the HAZ.

In single-stage welding, preheating creates thermal balance and reduces thermal gradients, thereby reducing stresses from thermal expansion and plastic deformation and consequently decreasing residual stresses and distortion. That is, while in multi-pass welding, in addition to the preheating temperature, the interpass temperature also affect thermal balance and gradient and must be kept near the preheating temperature [27].

For the present repair-welded gas turbine nozzle, since the repair area is relatively large and the heat input and the deposition rate are very low, it is difficult in practice to control the interpass temperature and keep it equal to the preheating temperature. Particularly for higher preheat temperatures, the difference between the interpass and preheating temperatures increases. Therefore, the preheating treatment may not work as expected and does not have a significant positive effect on the longitudinal residual stresses.

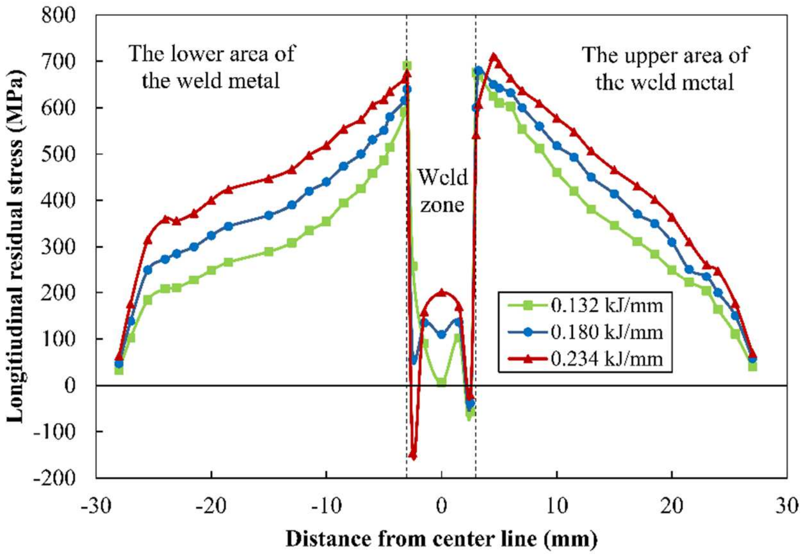

Fig. 13. Changes in longitudinal residual stresses along path 1 for different heat inputs.

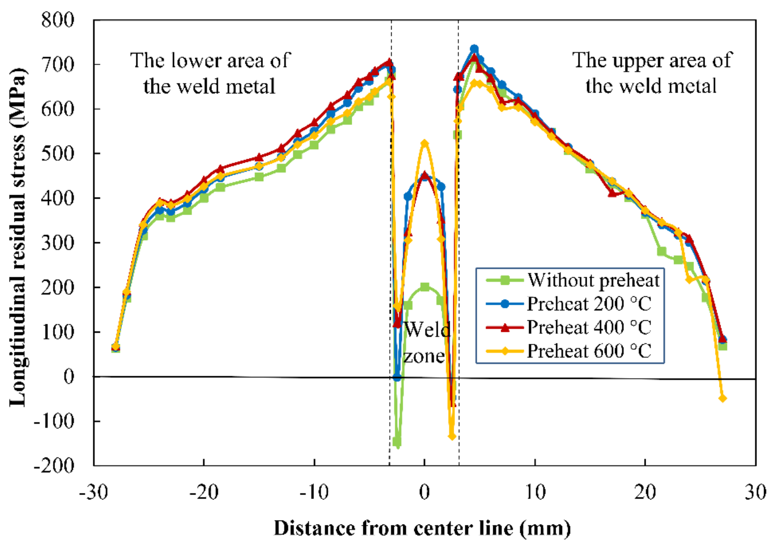

Fig. 14. Longitudinal residual stress distribution along path 1 for different preheating temperatures and a constant heat input of 0.234 kJ/mm.

On the other hand, due to the special and complex geometry of the nozzle and the welding area, the cooling of the part during the welding process is non-uniform. according to the temperature contours in Fig. 10, increasing the preheating temperature causes strong temperature gradients in the initial welding passes and increases the residual stresses in the area around the weld metal. In addition, the low heat transfer coefficient of the nozzle alloy (less than that for the carbon steels and stainless steels), may explain why preheating is less effective in reducing residual stresses compared to carbon steel and stainless-steel parts. Some other researchers who have studied the effect of the preheating treatment on the value of residual stresses in various welded joints have also reported the effectiveness of preheating treatment in reducing the residual stresses, in some of the cases [24, 28]. According to the results obtained in this section, for repair welding of the gas turbine nozzle made of IN738-LC superalloy, the use of preheating to reduce tensile longitudinal residual stresses is not suitable for multi-pass welding (i.e., repair of large-sized defects). In this case, the use of more advanced welding techniques such as superalloy welding to evaluate temperature (SWET) as an alternative to preheating treatment can be more effective [29].

5.2.3. *The effect of mechanical boundary conditions on the residual stresses*

Figure 15 shows the longitudinal residual stress profiles along path 1 for the constant heat input (0.234 kJ/mm) and different mechanical boundary conditions. As illustrated, using the clamps as mechanical restraints has led to an increase in the tensile longitudinal residual stresses in the center of the weld metal. Furthermore, the clamp with a higher contacting surface (i.e., Type I clamp) has a more detrimental effect and causes a further increase in the tensile longitudinal residual stresses in the center of the weld metal. According to the results shown in Fig. 15, the use of clamps does not influence the amount of tensile longitudinal residual stresses at the upper edge of the weld metal. However, as can be seen at the lower edge of the weld metal, the compressive residual stress is decreases as the contact surface of the clamps increases. The use of Type I and Type II clamps has reduced the compressive longitudinal residual stresses and increased the tensile longitudinal residual stresses at the lower edge of the weld metal. In this area, the highest tensile longitudinal residual stresses are related to the Type I clamps, with a value of 100 MPa.

According to the diagrams shown in Fig. 15, the major critical longitudinal tensile residual stress occurs in the HAZ (at a distance of about 4.5 mm from the center of the weld metal) at the upper half of the welded vane and is equal to about 710 MPa. When the Type I and Type II clamps are applied, the magnitudes of tensile longitudinal residual stresses at this point increase to 750 and 755 MPa, respectively. Based on the obtained results, the use of the Type I and Type II clamps has almost the same effect on the tensile longitudinal residual stresses in the HAZ and increases them up to 7% compared to the mode without clamps. The results of experimental and numerical studies conducted by other researchers [15, 30-34] showed that mechanical boundary conditions had a major effect on welding residual stresses.

5.2.4. *The simultaneous effect of mechanical boundary conditions and preheating on residual stresses*

Figure 16 shows the changes in the longitudinal residual stresses along paths 1 for the conditions of constant heat input (0.234 kJ/mm), utilizing Type II clamp and a preheating temperature of 400 ℃ (cases 3, 8, and 9).

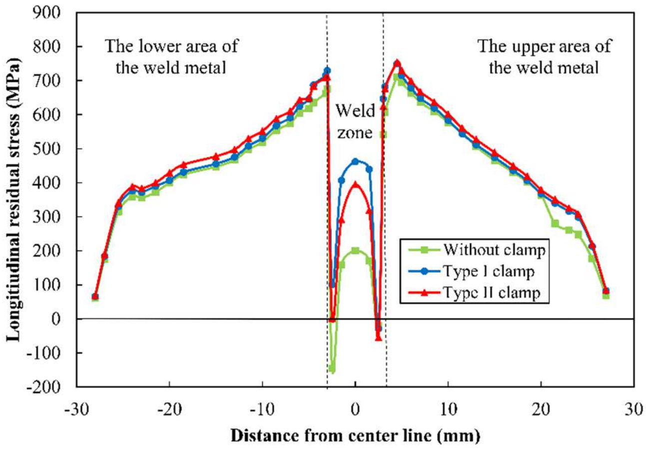

Fig. 15. Longitudinal residual stresses distribution along path 1 for different mechanical boundary conditions and a constant heat input of 0.234 kJ/mm.

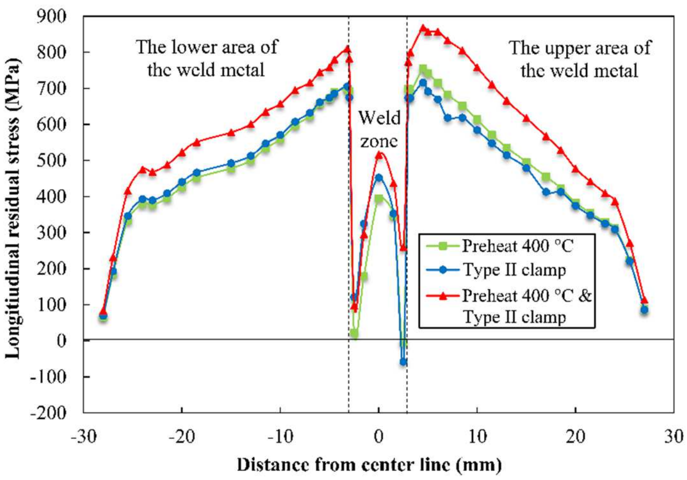

Fig. 16. Longitudinal residual stress distribution along path 1 for cases using only Type II clamps, only preheating at 400 °C, and the combined use of Type II clamps and preheating at 400 °C, all at a constant heat input of 0.234 kJ/mm.

According to the results presented in this figure, the simultaneous use of preheating and the Type II clamp has a more deleterious effect on tensile longitudinal residual stresses. As shown, the amount of tensile longitudinal residual stresses created in the HAZ near the trailing edge of the vane is greater than the yield strength of the nozzle material (the yield strength of IN-738LC at room temperature is 896 MPa [21]). Therefore, the aforementioned area is very susceptible to liquation cracking, strain-age cracking, and ductility-dip cracking.

5.2.5. *Mesh sensitivity analysis of the residual stresses obtained from numerical simulation*

To verify that the residual stress predictions are independent of mesh discretization, a mesh convergence study was performed for Case 9, which exhibits the highest thermal gradients and stress concentrations within the weld zone. The simulation was repeated using two additional refined mesh sizes in the weld zone: 0.4 mm and 0.3 mm, while keeping all other parameters constant. The 0.6 mm mesh served as the baseline. Table 6 presents the predicted peak longitudinal residual stress, the relative change compared to the 0.6 mm mesh, and the corresponding computational time for each mesh size. The results indicate that the predicted peak stress converges with mesh refinement. The relative change in peak stress between the 0.6 mm mesh and the two finer meshes (0.4 mm and 0.3 mm) is less than 3.5%. However, this marginal improvement in accuracy is accompanied by a substantial increase in computational cost: the runtime rises from 18 hours for the 0.6 mm mesh to 36 hours and 92 hours for the 0.4 mm and 0.3 mm meshes, respectively. Given the negligible gain in accuracy relative to the significant increase in computational time, a mesh size of 0.6 mm was selected for the parametric studies. This choice provides an optimal balance between achieving mesh-independent results and maintaining computational efficiency.

5.2.6. *Comparison of the residual stresses obtained from numerical simulation and experimental measurement*

Figure 17 shows the longitudinal residual stresses distribution along path 2 obtained by FE numerical simulation for the conditions of a heat input of 0.234 kJ/mm, a preheating temperature of 400 ℃, and Type II clamp (Case 9), along with the experimental measurement results of the longitudinal residual stresses at point B (Fig.9). From Fig. 17, it can be observed that there is relatively good agreement between the longitudinal residual stresses obtained by FE numerical simulation and those from experimental measurements at the desired point. However, there is a difference between the prediction and the measurement for this point at a distance of 17 mm from the weld center.

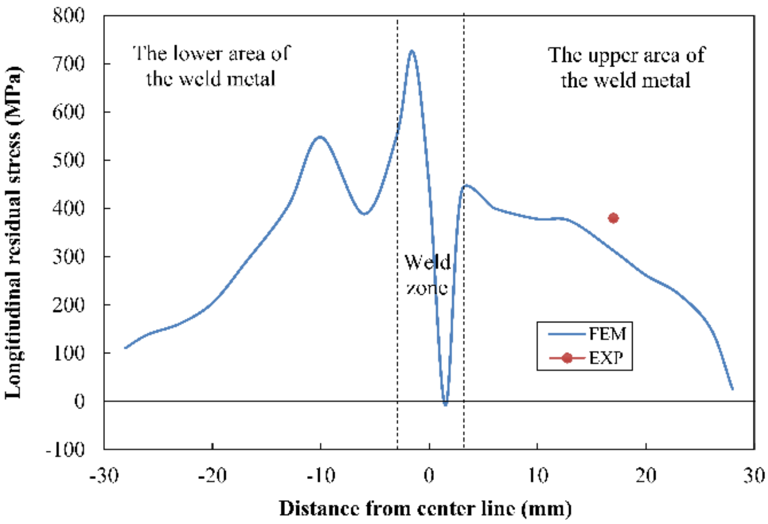

Fig. 17. Longitudinal residual stress distribution along path 2 for Case 9 welding conditions (heat input of 0.234 kJ/mm, preheating temperature of 400 °C, and Type II clamp) in comparison with experimental results.

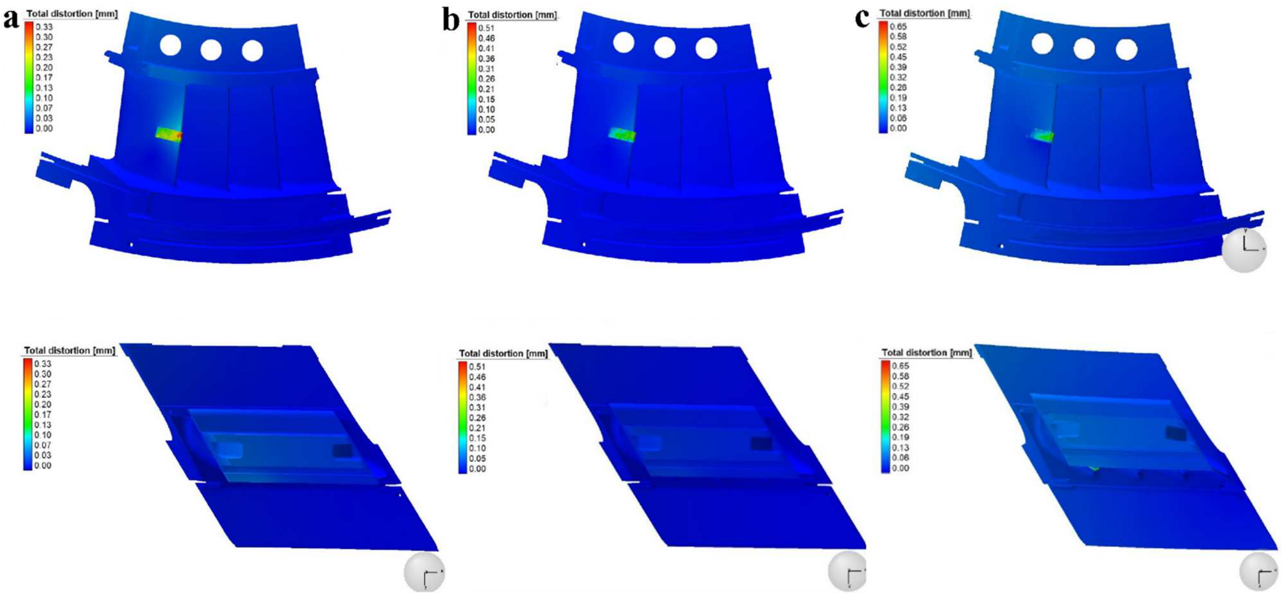

Fig. 18. The numerically predicted distortion for the repair welding at different heat inputs (a) 0.132 kJ/mm, (b) 0.18 kJ/mm, (c) 0.234 kJ/mm.

Table 6. Predicted peak longitudinal residual stress, relative change compared to the 0.6 mm baseline mesh, and computational time for each mesh size.

Mesh size (mm)	peak residual stress (MPa)	Change vs. 0.6 mm mesh.	computational time (hr)
0.6	723	—	18
0.4	745	3.0%	36
0.3	748	3.4%	92

Table 7. Comparison of longitudinal residual stress values obtained from FE numerical simulation and experimental measurements.

Distance from weld centre (mm)	Stress calculated by FEM (MPa)	Stress measured experimentally (MPa)	Error rate (%)
17	320	380	15.87

Based on the data shown in Table 7, for point B in Fig. 9, the difference between the longitudinal residual stress calculated by FE numerical simulation and the value obtained from experimental measurement is approximately 15.87%.

The difference between the results from FE numerical simulation and experimental measurement may be due to differences between the thermal and mechanical boundary conditions assumed in the simulation and those in the experiments, as well as the possible existence of residual stresses in the workpiece due to heat treatment before the repair welding process.

5.2.7. *The effect of heat input on the distortion*

The numerically predicted distortions after the final cooling of the nozzle welded at different heat inputs in front and bottom views are shown in Fig. 18. Figs. 18(a), (b), and (c) correspond to the welding process at heat inputs of 0.132 kJ/mm, 0.180 kJ/mm, and 0.234 kJ/mm, respectively. In the contours illustrated in Fig. 18, the distortion is shown using a gradient color scale. The dark blue and red colors represent the minimum and maximum distortion, respectively.

According to the results in Fig. 18, the distortion generated due to the repair welding of the nozzle is very small (less than 0.1 mm) for all welding heat inputs. For the nozzle welded at different heat inputs, the highest amount of distortion has been generated in the weld metal. This is related to the distortion of the elements in this area during the welding process and has no significant effect on the nozzle performance. A similar result has been reported by other researchers for the welding of gas turbine blades [7]. Thus, the variation of the welding heat input does not have a significant effect on the distortion of the repaired welded gas turbine nozzle.

5.2.8. *The effect of preheating on the distortion*

Figure 19 shows the numerically predicted distortion after the final cooling of the nozzles welded at a constant heat input (0.234 kJ/mm) and different preheating temperatures in front and bottom views. Figs. 19(a), (b), and (c) are related to cases 4, 5, and 6, respectively. Unexpectedly, the preheating treatment before the repair welding causes a significant increase in the distortion of the gas turbine nozzle compared to the non-preheated condition (Fig. 18c). According to the results presented in Fig. 19, the pattern of distortion is the same for the samples preheated at different temperatures, and as the preheating temperature, rises the distortion increases.

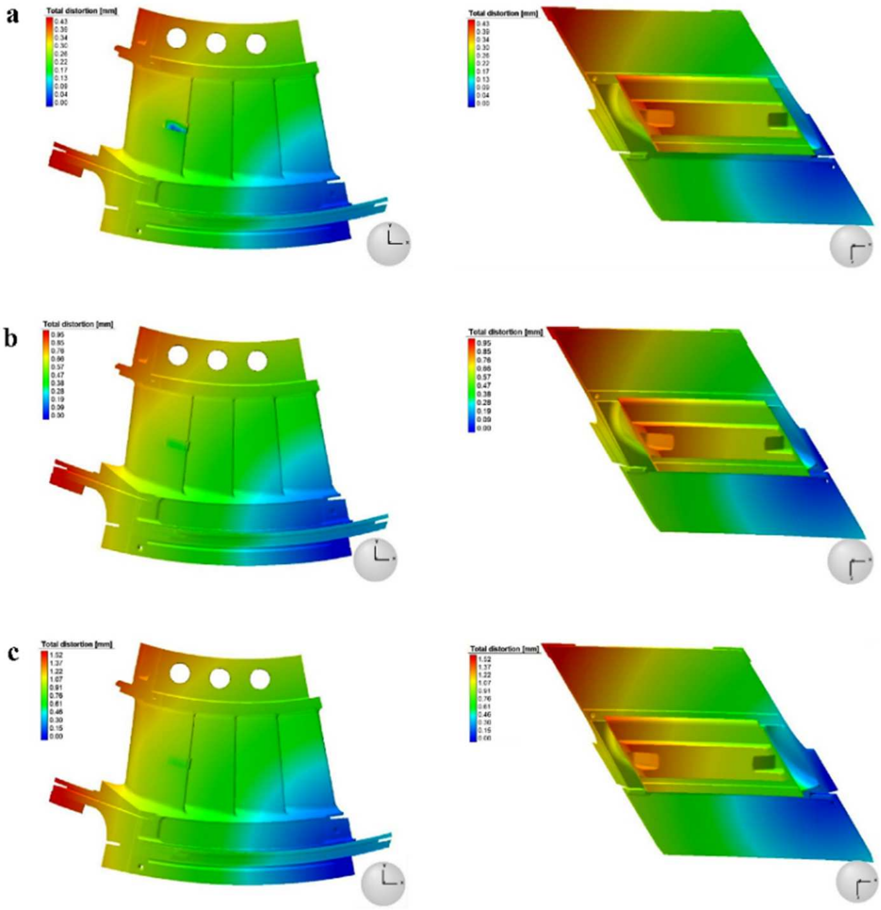

Fig. 19. The numerically predicted distortion for the repair welding with different preheating temperatures and a constant heat input of 0.234 kJ/mm (a) 200 °C, (b) 400 °C, and (c) 600 °C.

The increase in distortion resulting from the preheating treatment can be attributed to the complex geometry of the workpiece, which causes non-uniform cooling of the gas turbine nozzle after the repair welding process (Fig. 11). In addition, an increase in the preheating temperature further degrades the mechanical properties of the nozzle alloy, which in turn exacerbates distortion during cooling. As can be seen in Fig. 19, the greatest distortion occurs at the back left side of the nozzle platform (the red area), with values of 0.43, 0.95, and 1.52 mm for the preheating temperatures of 200 ℃, 400 ℃, and 600 ℃, respectively. Also, the amount of distortion in the upper left corner of the nozzle (the orange area) is greater than that at the other points. On the other hand, the least amount of distortion is found at the front right side of the nozzle platform (the blue area) and the distortion gradually increases with distance from this point. During the numerical simulation, the degrees of freedom of the four nodes in this area of the nozzle were set to zero.

5.2.9. *The effect of mechanical boundary conditions on the distortion*

Figure 20 illustrates the numerically predicted distortion after the final cooling of the nozzles welded at a constant heat input (0.234 kJ/mm) and in different mechanical boundary conditions in front and bottom views. Figs. 20(a) and (b) correspond to cases 7 and 8, respectively. Unexpectedly, the use of clamps —particularly clamp Type II— not only fails to decrease the distortion compared to the condition without using a clamp (Fig. 18(c)) but actually increases it.

The gas turbine nozzle deforms initially due to the application of these clamps. In addition to these initial deformations, thermal deformations occur in the welding process. After removing the clamps, a combination of these deformations takes place, leading the mechanical structure to a state of quasi-stationary equilibrium. The final distortion due to the superposition of initial deformations with thermal deformations depends on the clamp Type, the clamping force of the clamps, and the welding parameters.

When clamp Type I is used, the restricted displacement of the upper part of the nozzle causes non-uniform distortion, with greater distortion occurring in the unrestrained areas such as the nozzle platform (Fig. 20(a)). When clamp Type II is used, the restricted displacement of the front platform and the asymmetrical restrictions applied to one side of the nozzle, result in non-uniformity of the welding distortion in the part [7], and the distortion becomes even greater in the unrestrained areas such as the back nozzle platform and the upper part of the nozzle area (Fig. 20(b)). Therefore, the use of multi-directional clamps in the repair welding process of the gas turbine nozzle appears to be the only effective technique for reducing the distortion.

When clamp Type I is used, the restricted displacement of the upper part of the nozzle causes non-uniform distortion, with greater distortion occurring in the unrestrained areas such as the nozzle platform (Fig. 20(a)). When clamp Type II is used, the restricted displacement of the front platform and the asymmetrical restrictions applied to one side of the nozzle, result in non-uniformity of the welding distortion in the part [7], and the distortion becomes even greater in the unrestrained areas such as the back nozzle platform and the upper part of the nozzle area (Fig. 20(b)). Therefore, the use of multi-directional clamps in the repair welding process of the gas turbine nozzle appears to be the only effective technique for reducing the distortion.

5.2.10. *Comparing the distortion obtained from numerical simulation and experimental measurements*

The comparisons of the welding-induced distortion obtained by the finite element (FE) numerical simulation and the experimental measurements are shown in Fig. 21. The results are related to case 9 in Table 4, i.e., the welding with a heat input of 0.234 kJ/mm, a preheating temperature of 400 ℃, and the use of Type II clamp. As illustrated in Fig. 21, the experimentally measured displacements obtained by CMM match well with the FE numerical simulation predictions.

The relatively large difference between the experimental and FE numerical simulation results near the edges of the fusion zone (FZ) is not related to the distortion of the gas turbine nozzle. It is due to the excess molten material deposited on the edge of the welding zone, which can easily be removed by machining after the repair welding process. Both the experimentally measured and calculated results indicate that the highest and lowest distortion occur at the front and back platforms of the welded nozzle, respectively. For more accurate comparison, the distortion magnitudes obtained from experimental measurements and FE numerical simulation for six selected points on the surface of the welded nozzle (shown in Fig. 21(a)) are presented in Table 8.

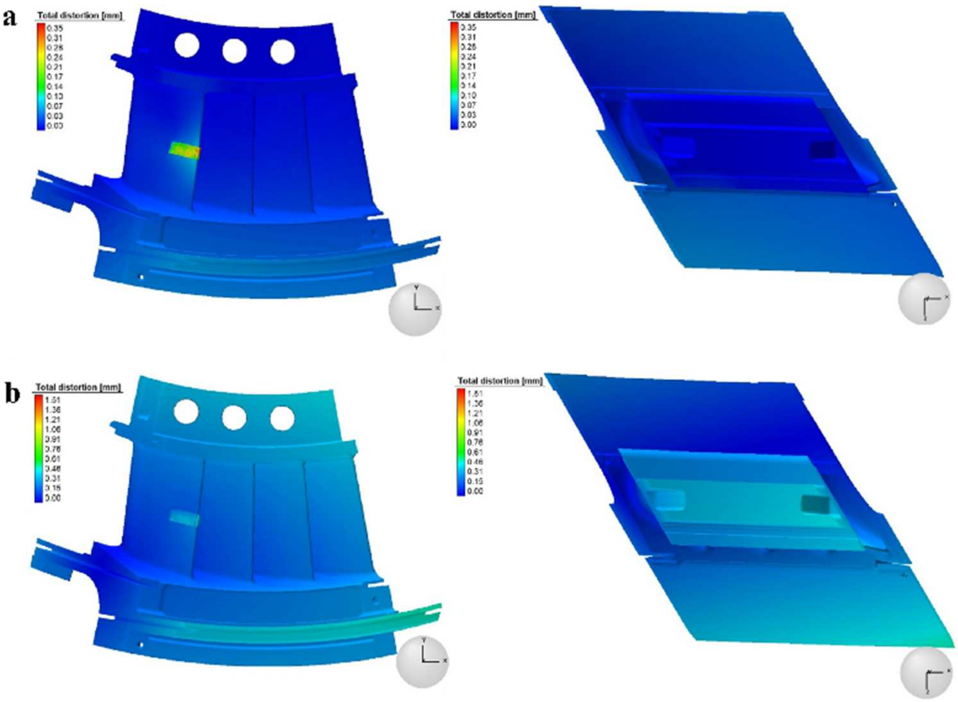

Fig. 20. The numerically predicted distortion for repair welding under different mechanical boundary conditions and constant heat input 0.234 kJ/mm (a) Type I clamp, (b) Type II clamp.

Table 8. Comparison of the distortion magnitude obtained from FE simulation and experimental measurements for the selected points on the surface of the welded nozzle marked in Fig. 20(a).

Point No.	FEM distortion (mm)	Experimental distortion (mm)	Error (%)
P1	0.11	0.13	15.38
P2	0.45	0.4	12.5
P3	0.44	0.39	12.82
P4	0.26	0.26	0
P5	0.44	0.4	10
P6	0.36	0.4	10

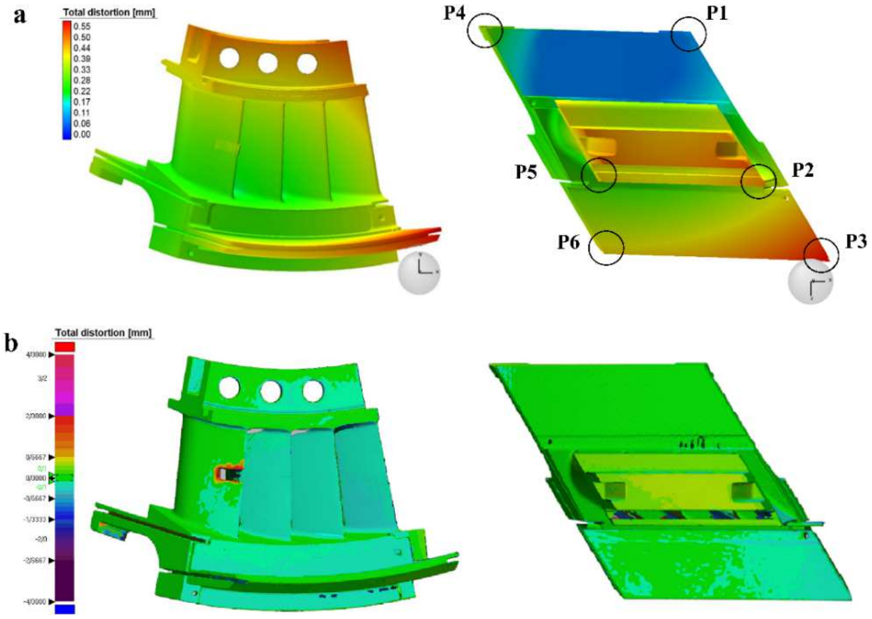

Fig. 21. Comparison between calculated and measured distortion for the gas turbine nozzle under case 9 welding conditions (heat input 0.234 kJ/mm, preheating temperature 400 °C, Type II clamp) (a) FE numerical simulation results, (b) experimental measurements by the CMM.

Based on the data shown in Table 8, the maximum deviation between the distortion magnitude obtained from experimental measurement and that calculated by FE numerical simulation is 15.4%, which occurs at point 1. The deviation between the results from the experimental measurement and those from the numerical simulation can be due to differences in the thermal and mechanical boundary conditions between the numerical simulation and the experiments.

6. Consistency of Numerical Simulation Results and Experimental Observations of Crack Formation in the Repair-welded Gas Turbine Nozzle

The results of the FPI test and visual examination performed on the repair-welded gas turbine nozzle, are presented in Fig. 22. The welding parameters were in accordance with case 9 of Table 4. As illustrated in Fig. 22, multiple cracks were observed along the heat-affected zone. The largest among them was a crack measuring approximately 2.5 mm in length, which had formed on the trailing edge of the welded vane at a distance of 1.5 mm from the weld metal.

The higher magnification images shown in Figs. 23(a), (b), and (c) indicate that the crack formed at the HAZ of the welded vane shows no significant signs of solidification cracks and appears to be a ductility dip crack. Precipitation-hardening nickel-based superalloys are prone to ductility dip cracking in the temperature range between the solidus (Ts) and 0.5 Ts due to the precipitation of γ' phase and a precipitous drop in ductility [29, 35].

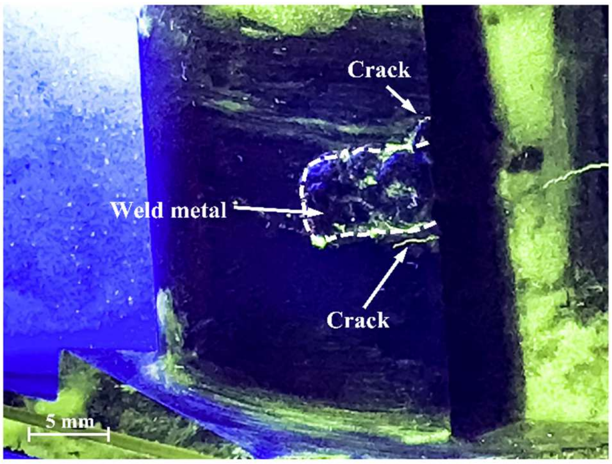

Fig. 22. Fluorescent penetrant inspection of the repair-welded area on the gas turbine nozzle.

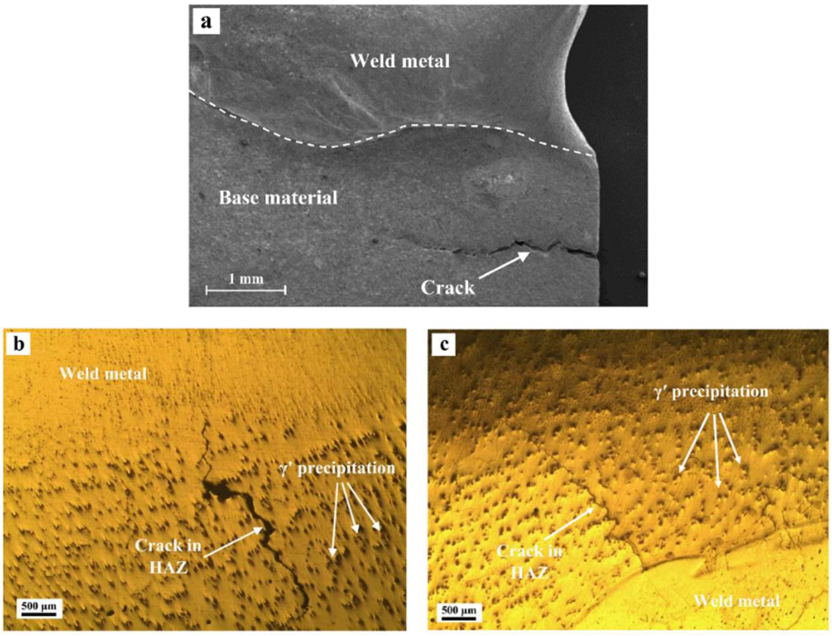

Fig. 23. (a) Image of the crack formed at the HAZ of the repair-welded vane of the gas turbine nozzle, and (b), (c) Micrographs of the region near the crack formed at the HAZ of the repair welded vane of the gas turbine nozzle showing γ' precipitates.

According to the temperature distribution obtained by FE numerical simulation (Fig. 24(a)), the cracked area on the trailing edge of the vane experiences a temperature range of 670–800 °C during the welding process. Additionally, based on the residual stress pattern shown in Fig. 24(b), the values of longitudinal residual stresses in the cracked area are in the range of 870 to 1050 MPa. Therefore, this area undergoes a critical stress condition (more than 95% of the yield stress of the base metal) and is thus susceptible to cracking. As a result, the necessary mechanical and metallurgical conditions for cracking were established simultaneously and led to the formation of the crack in the HAZ of the welded vane.

7. Conclusions

In this study, the residual stresses and distortion induced by multi-pass repair welding of an IN-738LC gas turbine nozzle guide vane were investigated through coupled thermo-mechanical FEM simulations validated by experiments. The following specific conclusions are drawn:

- The maximum tensile longitudinal residual stresses were consistently found in the heat-affected zone (HAZ) at the trailing edge of the nozzle vane, precisely matching the locations where cracks were observed experimentally. For heat input values of 0.132, 0.18, and 0.234 kJ/mm, the corresponding peak tensile stresses were 669, 680, and 710 MPa, respectively. This direct relationship between increased heat input, higher tensile residual stresses, and greater cracking susceptibility is expected to apply to other nickel-based superalloy components subjected to similar thermal and mechanical constraints.
- For this nozzle geometry, preheating did not significantly reduce tensile residual stresses and, unexpectedly, increased global distortion. This counterintuitive result stems from the nozzle's complex, asymmetric shape, which fosters uneven cooling under preheating conditions, combined with the inherently low thermal conductivity of IN-738LC. This observation should not be generalized to simpler geometries or alloys with higher thermal conductivity, where preheating may remain an effective mitigation strategy.
- The application of mechanical clamps increased the longitudinal residual stresses in the heat-affected zone by approximately 7% compared to the no-clamp condition and failed to reduce distortion. This outcome is largely due to the asymmetric restraint imposed by the clamps on the complex nozzle geometry. For symmetric components with balanced clamping, different results may be expected.
- According to the numerical results, for multi-pass repair welding of large-volume defects in variable-thickness IN-738LC nozzles, neither preheating nor conventional clamping alone is adequate to control residual stress and distortion. More advanced approaches—such as SWET welding or post-weld heat treatment—may be required.

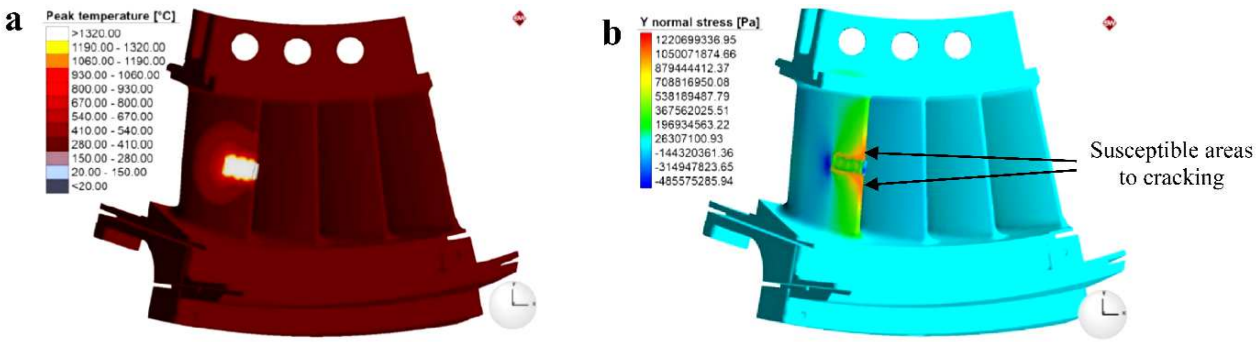

Fig. 24. Numerically predicted results related to the case 9 of the welding conditions, i.e., heat input of 0.234 kJ/mm, the preheating temperature of 400 °C, and the use of a Type II clamp (a) the peak temperature at each location during the repair welding process, (b) the distribution of longitudinal residual stresses.

Author Contributions

All authors contributed to the study conception and design. M.S. Rabie Zadeh was primarily responsible for the implementation of the numerical simulations and wrote the first draft of the article. E. Hajjari contributed to the design of the methods used and to the writing of the article. Data curation and validation were performed by S.M. Lari Baghal. A. Firouzian-Nejad contributed to obtaining funding for this project and revised the manuscript. All authors read and approved the final manuscript.

Acknowledgments

Financial support provided by National Iranian South Oil Company (NISOC) and Shahid Chamran University of Ahvaz through Grant No. SCU.EM98.581 is gratefully appreciated.

Conflict of Interest

The authors declare that they have no conflict of interest.

Funding

The National Iranian South Oil Company (NISOC) and Shahid Chamran University of Ahvaz supported this research.

Data Availability Statements

The datasets generated and/or analyzed during the current study are available from the corresponding author on reasonable request.

References

[1] Mourad, A.H., Almomani, A., Sheikh, I.A., Elsheikh, A.H., Failure analysis of gas and wind turbine blades: a review, *Engineering Failure Analysis*, 146, 2023, 107107.
[2] Monti, C., Giorgetti, A., Tognarelli, L., Mastromatteo, F., On the effects of the rejuvenation treatment on mechanical and microstructural properties of IN-738 superalloy, *Journal of Materials Engineering and Performance*, 26, 2017, 2244-2256.
[3] Peng, B., Xu, L., Chai, Z., Ba, F., Chen, X., Review of manufacturing technologies and materials in aeroengine turbine blade repair, *Journal of Materials Engineering and Performance*, 35, 2026, 10325-10348.
[4] Zhixin, Z., Wu, Z., Xiangde, B., Xiaodong, Z., Failure analysis of a first stage turbine blade made of directionally solidified GTD111 superalloy and repaired by welding process, *Engineering Failure Analysis*, 153, 2023, 107570.
[5] Durocher, J., Richards, N.L., Evaluation of the low heat input process for weld repair of nickel-base superalloys, *Journal of Materials Engineering and Performance*, 20, 2011, 1294-1303.
[6] Wang, H., Han, K., Peng, F., Zhang, B., Strain-age cracking in vacuum electron beam welded IN738LC alloy during post-weld heat treatment, *Vacuum*, 194, 2021, 110588.
[7] Bonakdar, A., Molavi-Zarandi, M., Chamanfar, A., Jahazi, M., Firoozrai, A., Morin, E., Finite element modeling of the electron beam welding of Inconel-713LC gas turbine blades, *Journal of Manufacturing Processes*, 26, 2017, 339-354.
[8] Ding, H., Zhang, W., Zhang, Z., Yin, D., He, W., Xie, D., Influence of welding sequences and boundary conditions on residual stress and residual deformation in DH36 steel T-joint fillet welds, *Thin-Walled Structures*, 204, 2024, 112337.
[9] Rohani Raftar, H., Khodabakhshi, A., Havia, J., Ahola, A., Skriko, T., Experimental and numerical study of welding-induced deformation and residual stress in 6082 aluminum: model validation and process design guidance, *Materials & Design*, 255, 2025, 114193.
[10] Ghafouri, M., Ahn, J., Mourujarvi, J., Bjork, T., Larkiola, J., Finite element simulation of welding distortions in ultra-high strength steel S960 MC including comprehensive thermal and solid-state phase transformation models, *Engineering Structures*, 219, 2020, 110804.
[11] Malschaert, D., Veljkovic, M., Maljaars, J., Numerical simulations of residual stress formation and its effect on fatigue crack propagation in a fillet welded T-joint, *Engineering Fracture Mechanics*, 306, 2024, 110236.
[12] Dong, P., Hong, J.K., Bouchard, P.J., Analysis of residual stresses at weld repairs, *International Journal of Pressure Vessels and Piping*, 82, 2005, 258-269.
[13] Song, S., Dong, P., Residual stresses at weld repairs and effects of repair geometry, *Science and Technology of Welding and Joining*, 22, 2017, 265-277.
[14] Zhao, L., Liang, J., Zhong, Q., Yang, C., Sun, B., Du, J., Numerical simulation on the effect of welding parameters on welding residual stresses in T92/S30432 dissimilar welded pipe, *Advances in Engineering Software*, 68, 2014, 70-79.
[15] Heinze, C., Schwenk, C., Rethmeier, M., Numerical calculation of residual stress development of multi-pass gas metal arc welding, *Journal of Constructional Steel Research*, 72, 2012, 12-19.
[16] Javadi, Y., Hasani, M., Sadeghi, S., Investigation of clamping effect on the welding sub-surface residual stress and deformation by using the ultrasonic stress measurement and finite element method, *Journal of Nondestructive Evaluation*, 34, 2015, 1-11.
[17] Sikstrom, F., Christiansson, A.K., Lennartson, B., Role of fixture forces on distortion in gas tungsten arc welding – an experimental and modelling approach, *Proceedings of the Institution of Mechanical Engineers*, Part B: Journal of Engineering Manufacture, 225, 2010, 140-148.
[18] Jiang, J., Yu, Y., Guo, Z.Y., Effect of welding heat input on residual stress and crack propagation in Q690CFD welded joints, *Journal of Constructional Steel Research*, 226, 2025, 109297.
[19] Danis, Y., Lacoste, E., Arvieu, C., Numerical modeling of inconel 738LC deposition welding: prediction of residual stress induced cracking, *Journal of Materials Processing Technology*, 210, 2010, 2053-2061.
[20] SIMUFACT Inc., SIMUFACT Welding Infosheets: Material, Version 4.0.3, 2014.
[21] Haynes International Inc., HAYNES 738 Alloy, Data Sheet, 2021. www.haynesintl.com/alloys/high-temperature-alloys/haynes-738
[22] Special Metals Corporation, Inconel Alloy 625, Data Sheet, 2020. www.specialmetals.com/assets/smc/documents/inconel-alloy-625
[23] Garcia-Garcia, V., Mejia, I., Reyes-Calderon, F., Benito, J.A., Cabrera, J.M., FE thermo-mechanical simulation of welding residual stresses and distortion in Ti-containing TWIP steel through GTAW process, *Journal of Manufacturing Processes*, 59, 2020, 801-815.
[24] Goldak, J.A., Akhlaghi, M., Computational Welding Mechanics, Springer, 2005.
[25] ASTM International, ASTM E837-20, Standard Test Method for Determining Residual Stresses by the Hole-Drilling Strain-Gage Method, West Conshohocken, PA, 2020.
[26] Ueda, Y., Murakawa, H., Ma, N., Welding Deformation and Residual Stress Prevention, *Elsevier Inc.*, 2012.
[27] Hou, F., Wan, N., Chang, Z., Chen, Z., Sun, H., An adaptive repair surface modeling approach for worn blades, *International Journal of Advanced Manufacturing Technology*, 94, 2018, 523-532.
[28] Charkhi, M., Akbari, D., Experimental and numerical investigation of the effects of the pre-heating in the modification of residual stresses in the repair welding process, *International Journal of Pressure Vessels and Piping*, 171, 2019, 79-91.
[29] DuPont, J.N., Lippold, J.C., Kiser, S.D., Welding Metallurgy and Weldability of Nickel-Base Alloys, *John Wiley & Sons*, 2009.
[30] Ma, N., Huang, H., Murakawa, H., Effect of jig constraint position and pitch on welding deformation, *Journal of Materials Processing Technology*, 221, 2015, 154-162.
[31] Ma, N., Huang, H., Yin, X., Guo, N., Welding distortion and inherent deformation under temporary tacking and its released states, *Science and Technology of Welding and Joining*, 21, 2016, 389-396.

[32] Rong, Y., Xu, J., Huang, Y., Zhang, G., Review on finite element analysis of welding deformation and residual stress, *Science and Technology of Welding and Joining*, 23, 2018, 198-208.
[33] Luo, Y., Gu, W., Peng, W., Jin, Q., Qin, Q., Yi, C., A study on microstructure, residual stresses and stress corrosion cracking of repair welding on 304 stainless steel: Part I-Effects of heat input, *Materials*, 13, 2020, 2416.
[34] Taraphdar, P.K., Kumar, R., Giri, A., Pandey, C., Mahapatra, M.M., Sridhar, K., Residual stress distribution in thick double-V butt welds with varying groove configuration, restraints and mechanical tensioning, *Journal of Manufacturing Processes*, 68, 2021, 1405-1417.
[35] Zhang, X., Chai, Z., Chen, H., Xu, J., Xu, L., Lu, H., Chen, X., A novel method to prevent cracking in directed energy deposition of Inconel 738 by in-situ doping Inconel 718, *Materials & Design*, 197, 2021, 109214.

ORCID iD

Mohammad Sajad Rabie Zadeh https://orcid.org/0009-0007-9003-8043
Esmaeil Hajjari https://orcid.org/0000-0001-5842-3741
Seyed Mohammad Lari Baghal https://orcid.org/0000-0002-6937-1825
Ahmad Firouzian-Nejad https://orcid.org/0000-0002-8631-7177

How to cite this article: Rabie Zadeh M.S., et al. Numerical simulation and experimental investigation of residual stress and distortion in the repair welding of a gas turbine nozzle guide vane, *J. Appl. Comput. Mech.*, xx(x), 2026, 1–18. https://doi.org/10.22055/jacm.2026.49060.5712